Simulations of Dielectric and Plasmonic Waveguide-Coupled Ring Resonators Using the Legendre Pseudospectral Time-Domain Method

Shih-Yung Chung, Chih-Yu Wang, Chun-Hao Teng, Chung-Ping Chen, *Member, IEEE*, and Hung-Chun Chang, *Senior Member, IEEE, Fellow, OSA*

***Abstract*—The accurate Legendre pseudospectral time-domain (PSTD) method is applied in this paper to the study of optical behaviors of 2-D dielectric and plasmonic waveguide-coupled ring resonators. Based on its inherent multidomain scheme with curvilinear-quadrilateral subdomain partitioning, the PSTD method possesses superior advantage in fulfilling field continuity conditions across material interfaces, which provides better numerical handling upon circular or even more complicated ring structures. Accordingly, investigations of several plasmonic nanoring resonators of different shapes with surface plasmon polariton (SPP) waves propagating on the metal/dielectric/metal waveguides are made with the aids of a well-fitted Drude–Lorentz material-dispersion model through analyzing their characteristics in the near-infrared and visible parts of the light spectrum. Especially, the racetrack-shaped ring is carefully designed with optimized track length to avoid the over- or under-coupling problem between the ring and input waveguides and, thus, achieve excellent spectral performance.**

***Index Terms*—Pseudospectral time-domain (PSTD) method, ring resonators, surface plasmon polaritons (SPPs).**

I. Introduction

THE ring resonator is a widely used optical device for filtering, switching, wavelength-division multiplexing (WDM), etc. [1]–[3]. Generally, it is designed to be with wide free spectral range (FSR), high finesse, and large extinction ratio, depending on the applications. But because of its high finesse, accurate resonant frequencies must be precisely evaluated; otherwise, the ring resonator will not be operated under the expected ON/OFF resonant conditions. Therefore, an accurate high-order algorithm is necessary and helpful to provide the required precise computations for the ring resonators. The finite-difference time-domain (FDTD) method using Yee mesh [1] has been a popular numerical analysis and simulation method adopted for computational electromagnetics in studying such structures and other plasmonic problems. However, due to its stair-casing approximation of the often occurring curved material interface, the FDTD calculation of the electromagnetic field near the curved interface is difficult to offer high precision under the Yee mesh. Additional efforts have to be paid for overcoming such stair-casing problem in the FDTD calculation, like the conformal scheme [4], the triangular mesh [5], the effective permittivity method [6], etc., but the accuracy is still restricted by the localized finite differences of fields.

On the contrary, a high-accuracy Legendre pseudospectral time-domain (PSTD) method which we utilize in this paper, with penalty scheme for solving Maxwell's equations, has been recently developed [7], in which the curved interface is treated carefully with a multidomain approach. In such scheme, the whole 2-D computational domain, including the perfectly matched layer regions, is partitioned into curvilinear-quadrilateral subdomains, which fit the curved interfaces [8] in the structure such that proper boundary conditions can be imposed through the penalty scheme, thus avoiding the stair-casing approximation as in the FDTD scheme. Besides, it could also provide high-accuracy computation, based on the high-order Legendre interpolation polynomials, for electromagnetic wave simulation. This PSTD method, therefore, would be quite suited for modeling ring resonators with circular or other complicated geometries.

In addition to simulating the classical dielectric waveguide-coupled ring resonators [9]–[12], herein we apply the PSTD method to further analyze the optical responses of the plasmonic waveguide-coupled ring structures, which were initially realized by Ebbesen and colleagues [13], operating under the phenomenon of surface plasmon polaritons (SPPs). After that, some other differently shaped ring structures were presented successively, like circular and air disk resonators [14], array of silver rods arranged in circle [15], sharp rectangular-ring structure [16], hexagonal-shape-ring structure [17], etc. Some of them will be simulated here for analyzing their behaviors by the PSTD method with well-fitted dispersive modeling, and their specific resonant behaviors based on plasmonic resonance with

Manuscript received September 01, 2011; revised December 21, 2011; accepted February 10, 2012. Date of publication February 24, 2012; date of current version April 06, 2012. This work was supported in part by the National Science Council of the Republic of China under Grant NSC99-2628-M-002-008 and Grant NSC99-2221-E-002-107-MY2, in part by the Excellent Research Projects of National Taiwan University under Grant 99R80306, and in part by the Ministry of Education of the Republic of China under "The Aim of Top University Plan" Grant.

S.-Y. Chung and C.-Y. Wang are with the Graduate Institute of Electronics Engineering and the Department of Electrical Engineering, National Taiwan University, Taipei 10617, Taiwan (e-mail: d95943006@ntu.edu.tw; d95943034@ntu.edu.tw).

C.-H. Teng is with the Department of Applied Mathematics and Center of Mathematical Modeling and Scientific Computing, National Chiao Tung University, Hsinchu 30010, Taiwan (e-mail: chunhao.teng@gmail.com).

C.-P. Chen is with the Graduate Institute of Electronics Engineering and the Department of Electrical Engineering, National Taiwan University, Taipei 10617, Taiwan (e-mail: cchen@cc.ee.ntu.edu.tw).

H.-C. Chang is with the Department of Electrical Engineering, the Graduate Institute of Photonics and Optoelectronics, and the Graduate Institute of Communication Engineering, National Taiwan University, Taipei 10617, Taiwan (e-mail: hcchang@cc.ee.ntu.edu.tw).

Color versions of one or more of the figures in this paper are available online at http://ieeexplore.ieee.org.

Digital Object Identifier 10.1109/JLT.2012.2188851

respect to structural shape will be shown, which are different from those of classical dielectric ring resonators. Besides, their poor spectral responses due to over- and under-couplings will be discussed and modified by an optimized racetrack ring.

The plasmonic waveguides, formed by metal/dielectric/metal (MDM) structures, have been widely studied nowadays, for they possess certain peculiar characteristics compared with traditional dielectric waveguides, such as subwavelength mode size [18]. In practice, the subwavelength-sized metallic waveguides would be useful in miniaturized integrated optical circuits. Furthermore, possible high transmittance of waves passing through the sharp bend [19] with low bending losses in such waveguide provides more flexibility and feasibility for manufacturing compact optical circuits and devices. Therefore, related plasmonic waveguide ring resonators could be manufactured with much smaller geometry than traditional dielectric rings. And simulations of such surface plasmon waves would demand high-accuracy near-field computations.

In the following, we will first explain some formulations about the PSTD method and the dispersive-material modeling which we used to curve-fit the dielectric constant of silver in visible and near-infrared wavelength regions in Sections II–IV. Then, in Section V, this accurate PSTD method will be utilized to study the electromagnetic responses of typical dielectric waveguide-coupled microring resonators and the results will be compared with those obtained from another high-order method, the discontinuous Galerkin time-domain (DGTD) method [9]. After that, the optical behaviors of the subwavelength plasmonic-ring resonators will be investigated. Both the Drude and the Drude–Lorentz material-dispersion models [1], [20] for approximating the actual silver characteristics [21] will be used for comparison. Several ring structures proposed in [14], [16], and [17] as well as one modified racetrack-type, or elongated, ring resonator will be analyzed and their electromagnetic responses in the visible and near-infrared regions will be presented.

II. Physical Equations and the Penalty Scheme

Electromagnetic fields in a linear, uniform, isotropic, and source-free medium region are governed by Maxwell's curl equations with constitutive relations

$$\nabla \times \mathbf{E} = -\frac{\partial \mathbf{B}}{\partial t}, \quad \nabla \times \mathbf{H} = \frac{\partial \mathbf{D}}{\partial t}, \quad \mathbf{D} = \varepsilon \mathbf{E}, \text{ and } \mathbf{B} = \mu \mathbf{H} \tag{1}$$

where ε is the permittivity and μ is the permeability. These equations can be rewritten in the following form for the convenience of further numeric implementation:

$$\bar{M}\frac{\partial \bar{q}}{\partial t} + \bar{A}_x\frac{\partial \bar{q}}{\partial x} + \bar{A}_y\frac{\partial \bar{q}}{\partial y} + \bar{A}_z\frac{\partial \bar{q}}{\partial z} = 0 \tag{2}$$

where the vector $\bar{q}$ and the matrices $\bar{M}$, $\bar{A}_x$, $\bar{A}_y$, and $\bar{A}_z$ will be specified for respective cases in the following subsections. For 2-D electromagnetic simulations, we will consider both transverse electric (TE) and transverse magnetic (TM) modes below.

A. Penalty Scheme

From the requirement of well-posed condition, it has been proved in [7] that the boundary conditions between any two adjacent subdomains can be fulfilled by adding a penalty term, which is proportional to $\bar{S}\bar{B}\bar{S}^T(\bar{q} - \bar{q}_{\rm bc})$, to (2). It can be found in [7] that $\bar{S}$ is the similarity transformation matrix for diagonalizing the symmetric matrix $\bar{A}$, which is defined by $\bar{A} = n_x\bar{A}_x + n_y\bar{A}_y + n_z\bar{A}_z$ with n_x, n_y, and n_z being the components of the unit normal vector to the subdomain boundary, and $\bar{B}$ is a diagonal matrix, in which the eigenvalues of matrix $\bar{A}$ are chosen and placed. A stable-in-time pseudospectral scheme for solving (2) can be constructed by choosing suitable proportionality parameter for the penalty term. The vectors, $\bar{q}$ and $\bar{q}_{\rm bc}$, in the penalty term mean the fields belonging to two adjacent subdomains, respectively, at the interface.

B. TE Modes

For TE waves in the xy plane with only H_x, H_y, and E_z field components, we have $\bar{q} = [H_x\ H_y\ E_z]^T$ and $\bar{M} = \text{diag}[\mu\ \mu\ \varepsilon]$ in (2). The spatial derivative indexes are expressed as

$$\bar{A}_x = \begin{bmatrix} 0 & 0 & 0 \\ 0 & 0 & 1 \\ 0 & 1 & 0 \end{bmatrix}, \quad \bar{A}_y = \begin{bmatrix} 0 & 0 & -1 \\ 0 & 0 & 0 \\ -1 & 0 & 0 \end{bmatrix}, \text{ and } \bar{A}_z = 0.$$

Therefore, the $\bar{S}$ matrix containing eigenvectors of matrix $\bar{A}$ for the penalty scheme will then become

$$\bar{S} = \frac{1}{\sqrt{2}}\begin{bmatrix} -n_y & \sqrt{2}n_x & -n_y \\ n_x & \sqrt{2}n_y & n_x \\ 1 & 0 & -1 \end{bmatrix}$$

with corresponding eigenvalues $\lambda = 1, 0$, and -1.

C. TM Modes

On the contrary, for TM waves in the xy plane having only E_x, E_y, and H_z field components, with which SPPs can exist and propagate at the metal/dielectric interface [18], we have $\bar{q} = [E_x\ E_y\ H_z]^T$ and $\bar{M} = \text{diag}[\varepsilon\ \varepsilon\ \mu]$. The spatial derivative indexes will then be

$$\bar{A}_x = \begin{bmatrix} 0 & 0 & 0 \\ 0 & 0 & -1 \\ 0 & -1 & 0 \end{bmatrix}, \quad \bar{A}_y = \begin{bmatrix} 0 & 0 & 1 \\ 0 & 0 & 0 \\ 1 & 0 & 0 \end{bmatrix}, \text{ and } \bar{A}_z = 0.$$

Similarly, the $\bar{S}$ can be derived from $\bar{A}$ as

$$\bar{S} = \frac{1}{\sqrt{2}}\begin{bmatrix} n_y & \sqrt{2}n_x & -n_y \\ -n_x & \sqrt{2}n_y & n_x \\ 1 & 0 & 1 \end{bmatrix}$$

with the same eigenvalues $\lambda = 1, 0$, and -1. Exchange between TE and TM modes can also be done by using electromagnetic duality, which would be the same as varying Maxwell's equations, the matrix $\bar{A}$, and the penalty terms.

III. Legendre Pseudospectral Method

In the multidomain Legendre pseudospectral method, each curvilinear subdomain in (x, y) coordinates can be mapped onto

a corresponding square region $[-1,1]\times[-1,1]$ in (ξ,η) coordinates through the transfinite blending method to construct the mapping functions $\xi=\xi(x,y),\eta=\eta(x,y)$ [8]. Spatially discretized points along the ξ axis, for example, are at grid points known as Legendre–Gauss–Lobatto (LGL) quadrature points with coordinates ξ_i s, in the interval $[-1,1]$ defined by the roots of the polynomial $(1-\xi^2)P'_N(\xi)$ in which the prime denotes derivative and P_N is the Legendre polynomial of degree N defined by

$$P_N(\xi)=\frac{1}{2^N N!}\frac{d^N}{d\xi^N}(\xi^2-1)^N. \tag{3}$$

Mathematically, an arbitrary function $f(\xi)$, which would be the electric field $\mathbf{E}$ and magnetic fields $\mathbf{H}$ in (1), can be approximated using degree-N Lagrange interpolation polynomials $l_j(\xi)$, based on the Legendre polynomial in (3), as

$$f(\xi)\approx\sum_{j=0}^{N}f(\xi_j)l_j(\xi) \tag{4}$$

with

$$l_j(\xi)=-\frac{(1-\xi^2)P'_N(\xi)}{N(N+1)(\xi-\xi_j)P_N(\xi_j)}.$$

Spatial derivative of this function $f(\xi)$ at the LGL quadrature point ξ_i can then be further approximated as

$$\frac{df(\xi_i)}{d\xi}\approx\sum_{j=0}^{N}\frac{dl_j(\xi_i)}{d\xi}f(\xi_j)=\sum_{j=0}^{N}D_{ij}f(\xi_j) \tag{5}$$

where D_{ij} is the N-dependent differential coefficient defined in [7]. In the same manner, spatial differentiations of electric and magnetic fields in (1) can be easily evaluated by multiplying the electromagnetic field vector by the differential matrix with elements D_{ij}. Besides, in order to maintain high accuracy as in spatial derivatives, the temporal differentiation (time-marching) is managed by the fourth-order Runge–Kutta scheme [22] instead of the leap-frog algorithm as generally used in the FDTD method [1].

IV. Models for Dispersive Materials

Before we analyze the plasmonic waveguide-coupled ring resonator, the modeling of dispersive metallic waveguide is discussed here. The dispersive characteristics of the metallic material in the optical wavelength range is modeled in this paper by both Drude and Drude–Lorentz models [1], [20], and their formulations can be written as

$$\begin{aligned}\varepsilon(\omega)&=\varepsilon_D+\sum_{n=1}^{2}\varepsilon_L\\&=\varepsilon_\infty-\frac{\omega_d^2}{\omega^2+i\omega\gamma_d}-\sum_{n=1}^{2}\frac{\Delta\varepsilon_{Ln}\omega_{Ln}^2}{\omega^2-\omega_{Ln}^2+i\omega\gamma_{Ln}}.\end{aligned} \tag{6}$$

Generally speaking, the curve-fitting is used to find out the suitable parameters that could properly match the measured experimental data, for instance, those reported in [21]. We use $\varepsilon_\infty=1.95,\omega_d=1.37\times10^{16}$ rad/s, and $\gamma_d=20\times10^{12}$ rad/s

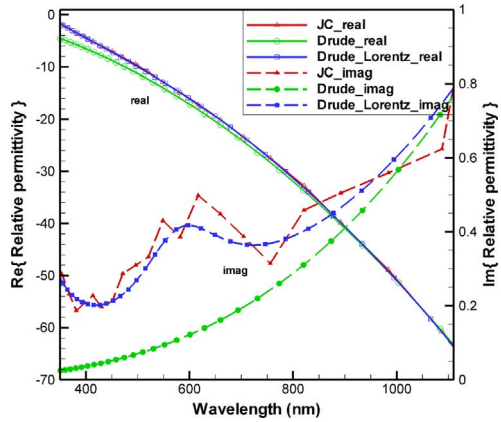

Fig. 1. Real and imaginary parts of the relative permittivity of silver depicted by experimental data (see [21]) and by the Drude and Drude–Lorentz models.

in this paper for silver in the Drude model, i.e., ε_D term only in (6). Because the Drude model provides only rough match to the actual metal, the modified Drude–Lorentz model [20] is utilized to improve the fitting by adding two additional Lorentz terms, i.e., adding the two ε_L terms to the Drude model expression as in (6). For establishing the Drude–Lorentz model with nine unknown parameters, we exploit the genetic algorithm and choose a proper curve-fit of these parameters for silver, obtaining $\varepsilon_\infty=1.0,\omega_d=1.3877\times10^{16}$ rad/s, $\gamma_d=1.87\times10^{13}$ rad/s, $\Delta\varepsilon_{L1}=0.089$, $\omega_{L1}=3.254\times10^{15}$ rad/s, $\gamma_{L1}=1.165\times10^{15}$ rad/s, $\Delta\varepsilon_{L2}=2.066$, $\omega_{L2}=7.758\times10^{15}$ rad/s, and $\gamma_{L2}=3.46\times10^{14}$ rad/s, which provide well fit in the optical wavelength range from 350 to 1100 nm as shown in Fig. 1, which reveals that the Drude–Lorentz model fits the dispersive characteristics of silver much better than the Drude model in this wavelength range, where the plasmonic phenomena are often concerned. Especially, the fluctuation of the imaginary part, which influences the plasmonic behaviors most, can be satisfactorily modeled.

By associating the polarization current with (6) and then applying the Fourier transform, the accompanying auxiliary differential equations (ADEs) [1] for both Drude and Lorentz models can be derived as

$$\frac{\partial\mathbf{J}_d}{\partial t}+\gamma_d\mathbf{J}_d=\varepsilon_0\omega_d^2\mathbf{E} \tag{7}$$

$$\frac{\partial^2\mathbf{J}_L}{\partial t^2}+\omega_L^2\mathbf{J}_L+\gamma_L\frac{\partial\mathbf{J}_L}{\partial t}=\varepsilon_0\Delta\varepsilon_L\omega_L^2\frac{\partial\mathbf{E}}{\partial t} \tag{8}$$

respectively, which are used to include the material dispersions in Maxwell's equations by adding the currents $\mathbf{J}_d$ and $\mathbf{J}_L$ in (2).

V. Simulation Results

Before analyzing ring resonators, numerical accuracy of the PSTD analysis of the straight dielectric waveguide is first examined, showing that the maximum absolute errors of fields are around 0.55, 0.1, 0.012, 0.001, and 0.0004 V/m for grid resolutions of subdomains corresponding to $N=10,12,14,16$, and 18 used, respectively, when the incident E_z field is normalized to 1 V/m. In the following, we will begin with the simulations of typical dielectric waveguide-coupled microring resonators and compare the results with those obtained using the DGTD method [9]. Then, several different subwavelength plasmonic

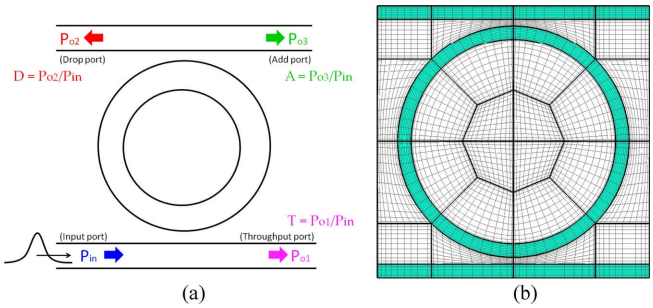

Fig. 2. Structure of the ring resonator. (a) Power transmittances at three ports. (b) Curvilinear domain partitioning and mesh grids based on LGL quadrature points.

waveguide-coupled ring resonators, which are formed based on the MDM waveguide structure, will be simulated and studied.

A. Dielectric Waveguide-Coupled Microring Resonators

We first consider the ring structure as shown in Fig. 2(a). The circularly shaped dielectric waveguide is placed between two straight ones, and the incident wave is excited from the left of the bottom waveguide. The "Input port," "Throughput port," "Drop port," and "Add port" are defined in Fig. 2(a), and power transmittance at each port can be obtained by normalizing the transmitted power at each port to the incident one. The ON/OFF resonant conditions are mainly influenced by the incident optical wavelengths, which would affect phase interferences inside the ring waveguide. In addition, waves traveling around the ring structure and being accumulated, when ON-resonance occurs, will be coupled down to the bottom waveguide and cause interference as well. Based on the curvilinear subdomain partitioning and LGL grid points, portion of the circular ring structure for analysis later is partitioned in Fig. 2(b) as an example.

The first ring case we discuss here is a dielectric single-ring structure, as shown in Fig. 2, studied in [10] with 2.5-μm radius and the gap between the circular and straight waveguides is 0.232 μm. The waveguide width is 0.3 μm with core of $\varepsilon_r = 10.24$ and air cladding. The FDTD method was adopted in [10] for computations and the obtained five ON-resonant orders (m's) and frequencies are listed in Table I together with those computed by the PSTD method. It is seen that the PSTD obtained frequencies are larger than the FDTD ones, with the differences ranging from 0.317 to 0.412 THz corresponding to the percentage differences from 0.17% to 0.20%. The PSTD computed free spectral ranges (FSRs), which are the differences between adjacent resonant dips, for the five modes are 50.63, 47.54, 44.79, and 42.15 nm; and the corresponding values obtained by the FDTD method [10] are 50.66, 47.56, 44.73, and 42.17 nm, respectively. The FDTD and PSTD computed quality factors (Q-factor), defined as $f_0/\Delta f$, where f_0 is the central frequency and Δf is the bandwidth, for the five resonant dips are also listed in Table I.

The next case is a ring resonator with the same geometry as that proposed in [9], which is again a single-ring structure as shown in Figs. 2 and 3. The dielectric waveguide is set to be 0.2-μm width with the dielectric constant $\varepsilon_r = 9$ placed in free space. The radius of the ring is $R = 1.7$ μm, and the gap between the ring and the straight waveguide is 0.1 μm. Both our

TABLE I
COMPARISON OF FIVE CALCULATED RESONANT FREQUENCIES AND Q-FACTORS BETWEEN THE FDTD AND PSTD METHODS

m	FDTD (THz)	PSTD (THz)	difference	Q (FDTD)	Q (PSTD)
25	185.85	186.170	0.172%	3700	3800
26	191.88	192.213	0.173%	5000	4400
27	197.90	198.256	0.180%	4000	4700
28	203.92	204.308	0.190%	4000	5200
29	209.94	210.351	0.196%	4000	5400

PSTD and the DGTD [9] calculated transmittance spectra are depicted in Fig. 3(a) and (b) for the "Throughput port" and the "Drop port," respectively. There are no waves propagating to the "Add port" under this single-ring structure, thus the transmittance spectra at the "Throughput port" and the "Drop port" would be totally complementary. Notice that the transmittance spectrum at the "Throughput port" is decreasing at the lower frequency (longer wavelength) range. This can be possibly explained by two closely coupled waveguides near the gap, where one waveguide is straight and the other is curved. For shorter wavelengths, two waves, one from the straight waveguide and the other from the ring, propagating with the same phase velocities, can interfere comparably, but waves at longer wavelengths cannot. In other words, one can imagine that there is a short section of the waveguide just near the gap where the curved waveguide can also be treated as a straight one, such that one full wave cycle of shorter wavelength can be totally situated inside, but the wave of longer wavelength cannot. Therefore, waves at longer wavelengths (lower frequencies) would have more incomplete interferences at the gap and leave some residual waves in the ring, which will keep going around the ring and be coupled out to the "Drop port," corresponding to transmittances of about 16%, as shown at lower frequencies in Fig. 3(b).

The PSTD and DGTD results in Fig. 3(a) and (b) are seen to almost overlap with each other. The slight difference is examined by checking the resonant frequency at 226.4 THz. This frequency was considered in [9] to check numerical convergence. Our PSTD result is found to be smaller by 0.1 THz, or 0.045%. When examining this resonant dip for different grid resolutions, it can be seen that the position of the dip remains the same as N (i.e., $(N+1)\times(N+1)$ grid points in each subdomain) increases in the PSTD method, as depicted in Fig. 3(c). The DGTD calculated convergence behavior for this dip as presented in [9, Fig. 6(b)] is plotted in Fig. 3(d) in which the PSTD result is also plotted. It is seen the dip moves to left in the DGTD method as Δx is decreased and converges to a frequency value which is about 0.1 THz (or 0.045%) larger than the PSTD's dip frequency, Such small percentage difference is nevertheless four times better than the differences between the PSTD and FDTD calculations as given in Table I. The PSTD computed Q-factors for the five resonant dips in Fig. 3(a), from left to right, would be 82, 108, 141, 180, and 227, respectively; and the FSRs are 62.7, 57.7, 53, and 49.1 nm.

The field distributions of the ON/OFF resonances at 245.317 and 249.827 THz are depicted in Fig. 3(e) and (f), respectively, for this single-ring case. Because the transmitted power is zero at the "Throughput port," and 100% at the "Drop port" for the

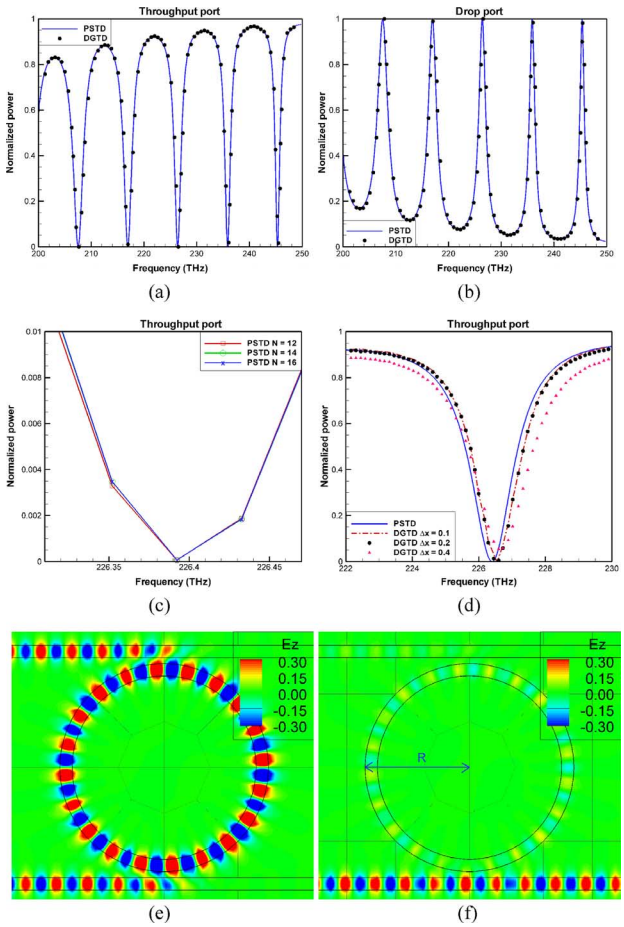

Fig. 3. Single-ring resonator. (a) Power transmitted to the "Throughput port." (b) Power transmitted to the "Drop port." (c) Resonant dips for different N s by the PSTD method. (d) Resonant dips for different grid resolutions by DGTD method in comparison with the PSTD's result. (e) ON-resonance at 245.317 THz. (f) OFF-resonance at 249.827 THz.

ON-resonance condition as shown in Fig. 3(a) and (b), there is no wave propagating downward to the right of the bottom waveguide, but turning along the ring to the left of the upper waveguide. Stronger fields are found to be accumulated inside the ring waveguide because of the in-phase interference. As a result, part of these strong fields inside the ring will be coupled to the bottom waveguide, completely canceling, by destructive interference, the incident waves propagating toward the right, while part will be coupled to the upper waveguide and propagates to the left. On the other hand, about 97% of the power is transmitted to the "Throughput port" and only 3% to the "Drop port" for the OFF-resonance condition. Apparently, there would be no strong fields accumulated inside the ring structure due to that waves traveling around the ring waveguide cancel the waves newly coupled into the ring. Therefore, there are not enough waves inside the ring, as shown in Fig. 3(f), which could be further coupled to the bottom waveguide and cause interferences. Notice that the electric field profiles are shown in Fig. 3(e) and (f) using smaller scale (-0.3–0.3 V/m) in order to display small fields.

Another ring resonator presented in [9] is a double-ring structure in which two rings stack along the y axis as shown in Fig. 4. The structural parameters for the double-ring are the same as

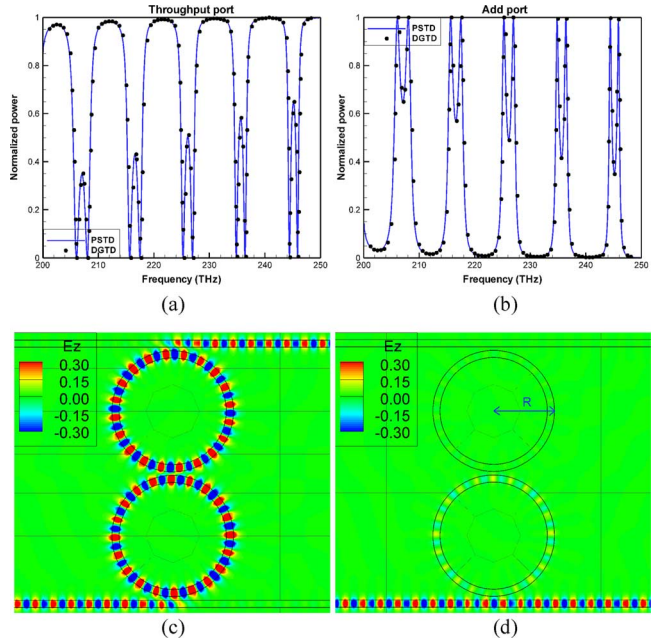

Fig. 4. Double-ring resonator. (a) Power transmitted to the "Throughput port." (b) Power transmitted to the "Add port." (c) ON-resonance E_z distribution at 245.861 THz. (d) OFF-resonance E_z distribution at 249.827 THz.

those for the single-ring. Similarly, the transmittance spectra at the "Throughput port" and the "Add port" are simulated by the PSTD method and shown in Fig. 4(a) and (b), respectively, along with the corresponding DGTD results. Now, it can be seen that the transmitted powers become zero at the "Drop port" instead because the upper ring turns the wave to the "Add port," such that results in Fig. 4(a) and (b) will be totally complementary. These PSTD computed spectra are also shown to almost match the corresponding results by the DGTD method in [9]. Note that the transmittance in Fig. 4(a) for the double-ring structure is also smaller in the lower frequency region, but this decrease is less than that in the single-ring structure. It is because there are two curved waveguides at the center gap between the two rings, which would cause the coupling interferences less efficient for longer wavelengths and thus somewhat keep the waves from propagating to the upper ring and further coupling outward to the "Add port," as shown in Fig. 4(d). Besides, each resonant dip in the single-ring case is now split into two sub-dips in the double-ring resonator case, in which odd and even modes are formed.

Field distributions of ON- and OFF-resonances at frequencies 245.861 and 249.827 THz for the double-ring resonator are shown in Fig. 4(c) and (d), respectively. It can be seen that the mode field in Fig. 4(c) is odd, or antisymmetric, with respect to the centerline between the two rings, and that of another dip at 244.417 THz is even, or symmetric, instead. From the shown behaviors of ON- and OFF-resonances, this double-ring structure, intuitively, can be used as a switch such that waves with specific wavelengths, i.e., ON-resonant wavelengths, will propagate along the upper waveguide while some other wavelengths, i.e., OFF-resonant wavelengths, will go through the bottom waveguide instead. In addition, this double-ring resonator can certainly be cascaded further and used as a WDM device to separate waves composed of many wavelengths.

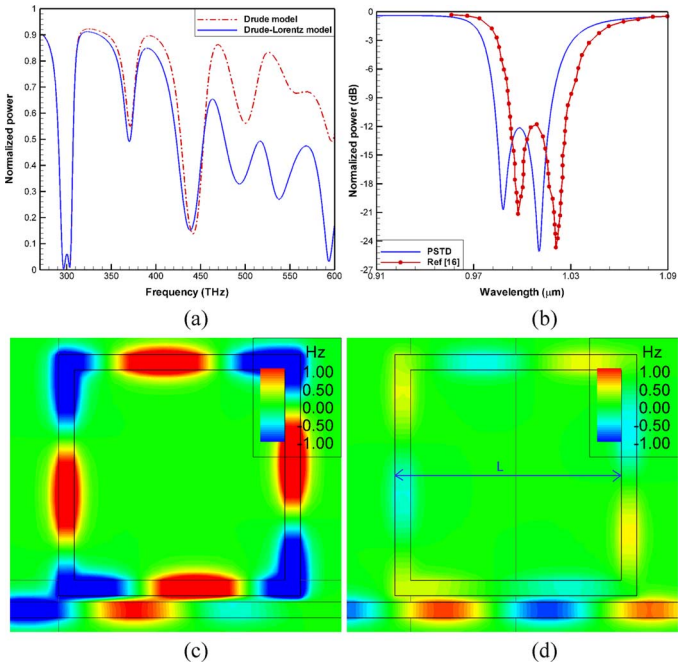

Fig. 5. PSTD simulation results for the rectangular-shaped MDM ring resonator. (a) Transmittance spectra. (b) Comparison with [16] with the ordinate of the spectral plot in dB scale. (c) ON-resonance H_z distribution at 296.72 THz. (d) OFF-resonance H_z distribution at 322.3 THz.

B. MDM Plasmonic Square-Shaped Ring Resonators

In the following, we apply the PSTD method to study several plasmonic waveguide-coupled ring resonators. It is known that the SPPs can be guided and propagate at the metal/dielectric interface only under the TM mode with E_x, E_y, and H_z fields in the xy plane [18]. So in the following, we will consider the TM modes. Also, the plasmonic waveguides we consider here are made of the MDM structure, in which the insulator region is taken to be air.

The "notch" filter type ring resonators with upper waveguide removed will be considered below, since plasmonic waveguides suffer much larger losses than typical dielectric waveguides, especially in the wavelength range of visible light. We have mentioned that, for ON-resonance condition of the "dielectric" ring resonator, part of the accumulated strong electromagnetic waves inside the ring will be simultaneously coupled to both the upper and bottom waveguides. But in the case of ON-resonance condition of the "plasmonic" ring resonator, the waves inside the ring decay quickly when traveling around the ring structure. Therefore, removing the upper waveguide can help saving more waves inside the ring so that they can be accumulated high enough to totally cancel the incident wave at the bottom waveguide, and high extinction ratio can be maintained.

The first plasmonic ring resonator to be discussed is a square-shaped structure with edge length $L = 725$ nm and waveguide width $W = 50$ nm, which was first proposed in [16] and simulated with the FDTD method. The gap between the ring structure and the bottom waveguide is 20 nm. It is well known that a dielectric waveguide cannot have such sharp bend because of accompanied large bending losses. But sharp bends of plasmonic waveguide have been shown to be able to provide possible high transmittance of waves with low bending losses

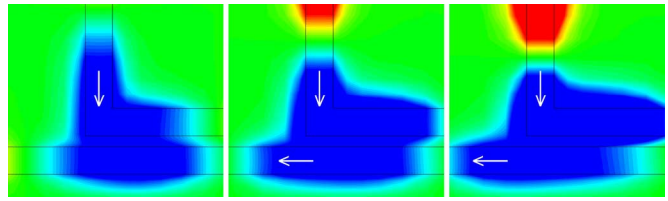

Fig. 6. Evolution of fields after the incident wave terminated for monitoring the backward propagating wave in the ring resonator of Fig. 5.

[19], making this square-shaped ring possible. The transmittance spectra of the "Throughput port" are depicted in Fig. 5(a) within the frequency range of 270–600 THz. In Fig. 5(a) and the following similar figures, the dashed line (red) and the solid line (blue) correspond to results obtained with the Drude and the Drude–Lorentz model, respectively. Although our Drude–Lorentz model fitting can support up to about 850 THz, frequencies over 600 THz are omitted because the extinction ratio of transmittance is poor due to larger losses in metal. From Fig. 5(a), it can be seen that there are two workable resonant dips near 300 THz, and others are not good enough to be used because of their insufficient extinction ratios and low finesse. The transmittance spectra near 300 THz would be similar to those in [16] if the ordinate is plotted in dB scale, as shown in Fig. 5(b), but with about 3.35 THz spectral shift or about 1.14% difference between our PSTD results and those of [16]. Apparently, this difference is much larger than that in the case of dielectric-ring. Therefore, accurate numerical spectral calculations should be more essential for plasmonic-ring structures. The field distribution at the first dip, i.e., the ON-resonance, occurring at 296.72 THz and that at the OFF-resonance at 322.3 THz are shown in Fig. 5(c) and (d), respectively.

From the ON-resonant result in Fig. 5(c), one can observe that no waves are propagating toward the "Throughput port," and the waves at the "Input port" are enhanced. It is because the waves inside the ring split when coupling to the bottom waveguide. That is to say, when waves travel along the last vertical waveguide of the ring structure, perpendicular coupling forces part of the waves to go to the left and part to the right. Then, waves propagating to the right would cancel, by destructive interference, the incident waves while those to the left would enhance, by constructive interference, the incident waves.

To observe this backward propagating wave, the field evolution at the lower left corner after termination of the incident wave is illustrated in Fig. 6 for three time steps, showing the left propagating wave as time marches. Note that the upper waveguide is removed so that the resonator becomes of the notch type; otherwise, part of waves would uncontrollably propagate to the "Add port," as what occurring at the bottom waveguide depicted in Fig. 6.

There are totally six dips with transmittances less than 50% in Fig. 5(a) at frequencies 296.72, 303.345, 438.523, 493.648, 537.777, and 593.588 THz. Their corresponding H_z field distributions are shown in Fig. 7(a)–(f), respectively. Except that more cycles of waves are able to be situated inside the ring structure as the frequency increases, one can find some regular patterns of symmetry in these figures since the establishment of resonant modes have to fit the structure shape. This will become more apparent in the next example.

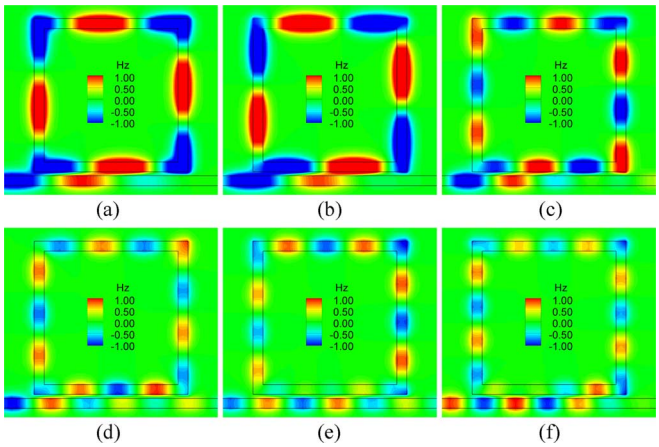

Fig. 7. PSTD simulation results for the rectangular-shaped MDM ring resonator, showing the H_z distributions at six resonant dips in Fig. 5(a) at (a) 296.72 THz, (b) 303.345 THz, (c) 438.523 THz, (d) 493.648 THz, (e) 537.777 THz, and (f) 593.588 THz.

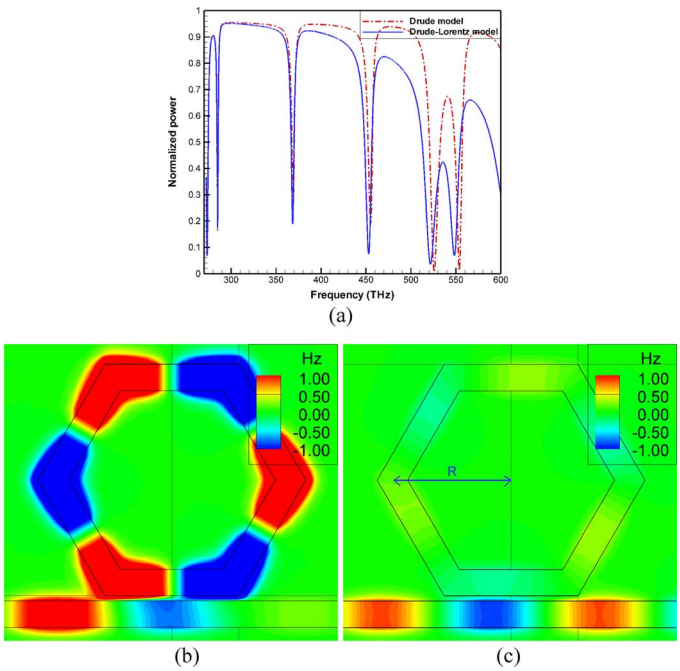

Fig. 8. PSTD simulation results for the hexagonal-shaped MDM ring resonator. (a) Transmittance spectra. (b) ON-resonance H_z distribution at 273.41 THz. (c) OFF-resonance H_z distribution at 296.2 THz.

C. MDM Plasmonic Hexagonal-Shaped Ring Resonators

Disadvantage of the rectangular-shaped ring resonator lies obviously in its sharp (90°) waveguide coupling, which would cause excessive backward propagating waves to the "Input port." Also, the transmittance of waves passing through the sharp bend has been shown to be worse as the wavelength becomes shorter than 1 μm [19]. Later, Han *et al.* proposed a modified hexagonal ring structure [17], as shown in Fig. 8. This hexagonal geometry smoothes the bend angle to 60°, and thus leads to a smoother directional waveguide coupling, which means that waves can be coupled following the tilted waveguide direction and reduce backward propagating waves to the "Input port." The plasmonic waveguide used was of

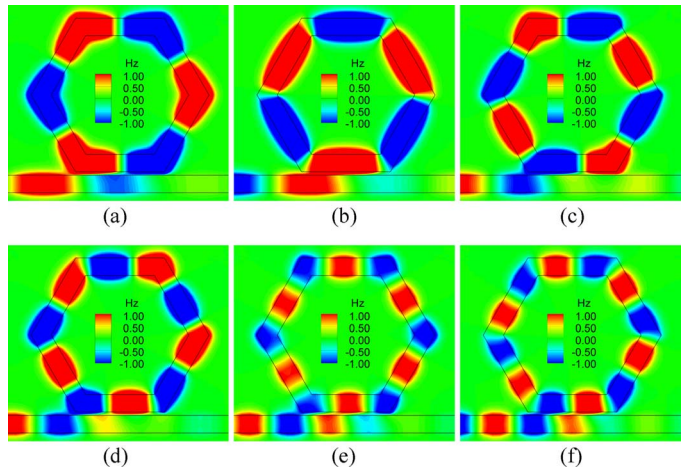

Fig. 9. PSTD simulation results for the hexagonal-shaped ring, showing the H_z distributions at five resonant dips in Fig. 8(a) at (a) 273.41 THz, (b) 285.06 THz, (c) 368.49 THz, (d) 453.146 THz, (e) 521.614 THz, and (f) 548.347 THz.

width $W = 100$ nm, the ring radius $R = 450$ nm as indicated in Fig. 8(c), and the gap between the ring structure and the bottom waveguide was 20 nm. The transmittance at the "Throughput port" is shown in Fig. 8(a), which is of better extinction ratio and higher finesse for each resonant dip than in the rectangular-shaped ring structure. The field distributions of the ON-resonance at 273.41 THz and the OFF-resonance at 296.2 THz are shown in Fig. 8(b) and (c), respectively. One can observe that the coupled waves are still somewhat propagating backward to the "In-put port" for ON-resonance in Fig. 8(b) so that field enhancement appears.

Similarly, field distributions at six dips with transmittances less than 50% in Fig. 8(a) corresponding to resonant frequencies 273.41, 285.06, 368.49, 453.146, 521.614, and 548.347 THz are shown in Fig. 9(a)–(f), respectively. One can see that the peaks and troughs in Fig. 9(a) are all at the corners, and those in Fig. 9(b) are all shifted to the middles of the ring edges. These two dips can be regarded as nearly degenerate modes since the fields in Fig. 9(a) are distributed symmetrically with respect to the 120° lines, while those in Fig. 9(b) are distributed antisymmetrically, with both having three wave cycles inside the ring. Likewise, the profiles in Fig. 9(e) and (f), with six wave cycles inside the ring, possess similar symmetric and antisymmetric field distributions. According to the above observations and discussion, the occurrence of resonance would depend not only on the circumference of the ring but also on the arrangement of corners and edges in the ring, which affect the locations of the field peaks and troughs. These behaviors are quite different from those of the dielectric circular-ring resonator. In fact, waves inside the (circular) dielectric ring are propagating waves and those inside the plasmonic ring are standing waves due to the waveguide corners or bends. But for the double-ring resonator discussed in connection with Fig. 4, similar degenerate modes can occur, as evidenced by the split resonant dips and peaks in Fig. 4(a) and (b) due to the coupling interference between the two rings. With the same number of wave periods in the two rings, the two degenerate modes would have symmetric and antisymmetric field distributions, respectively, with respect to the centerline between the two rings.

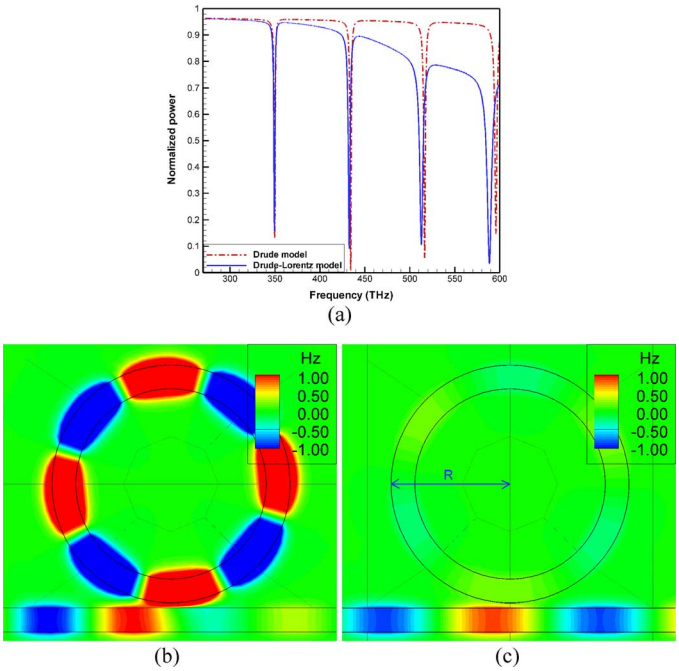

Fig. 10. PSTD simulation results for the circular-shaped MDM ring resonator. (a) Transmittance spectra. (b) ON-resonance H_z distribution at 349.4 THz. (c) OFF-resonance H_z distribution at 272.53 THz.

D. MDM Plasmonic Circular-Shaped Ring Resonators

The problem of backward propagating waves and resultant worse spectral responses appearing in above two ring-resonator cases is apparently due to the existence of corners and the excessively long coupling length in the rings, which can possibly be reduced by restoring to the typical circular ring shape. Fig. 10 shows our simulation results for a circular-shaped ring structure with the plasmonic waveguide of width $W = 100$ nm and ring radius $R = 500$ nm, which are chosen for comparison with the hexagonal-shaped ring one. The gap between the ring structure and the bottom waveguide is still 20 nm. From the transmittance spectra in Fig. 10(a), however, it can be deduced that the coupling length is too short to provide enough coupling interferences for the resonant dips to be with better extinction ratios. The field distributions at the first dip, i.e., ON-resonance, occurring at 349.4 THz as well as the OFF-resonance at 272.53 THz are shown in Fig. 10(b) and (c), respectively.

E. MDM Plasmonic Racetrack-Shaped Ring Resonators

The insufficient coupling length of circular ring can be improved by simply adding two sections of straight waveguide into the circular ring, resulting in the racetrack, or elongated [1], type ring structure. But for the coupling of waveguides, we know that the length of the straight waveguide should be well designed, or the problem of over-coupling or under-coupling, as seen in aforementioned cases, will occur and worsen the spectrum again. Therefore, we have done numerical experiments by varying the straight-waveguide length from 0 to 200 nm, and the calculated normalized powers at the four resonant dips in Fig. 10(a) are depicted in Fig. 11 with respect to the straight-waveguide length added. Apparently, there is an optimized straight-waveguide length near 100 nm such that longer

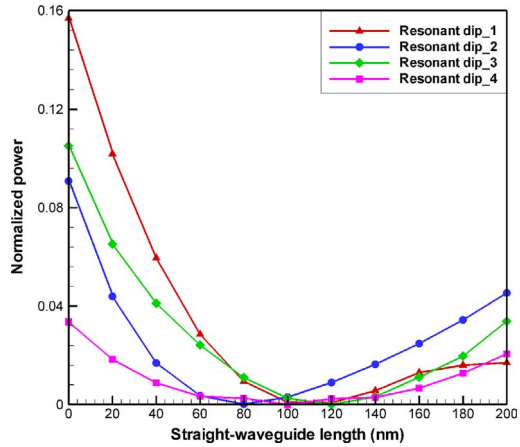

Fig. 11. Normalized powers at four resonant dips in Fig. 10(a) versus the straight-waveguide length in the racetrack-shaped ring.

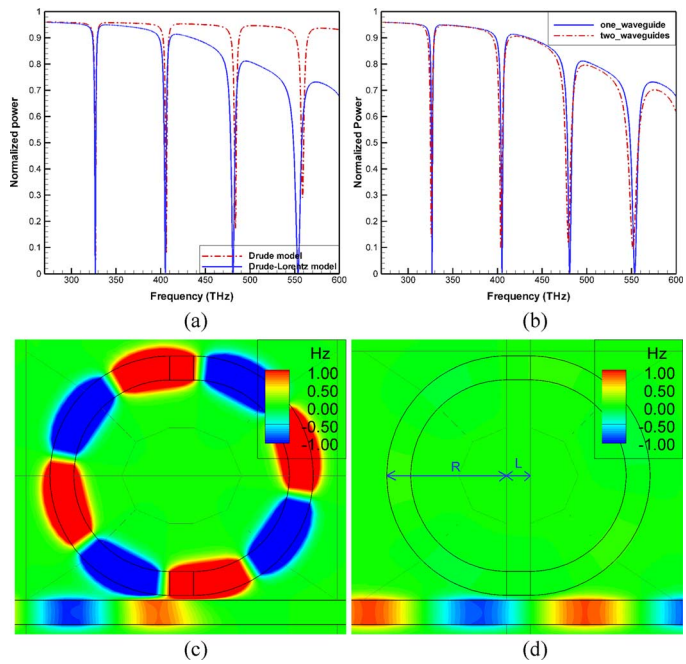

Fig. 12. PSTD simulation results for the racetrack-shaped MDM ring resonator. (a) Transmittance spectra. (b) Comparison of transmittance spectra between one- and two-waveguides. (c) ON-resonance H_z distribution at 326.73 THz. (d) OFF-resonance H_z distribution at 272.53 THz.

or shorter length would cause lower extinction ratios. This study can also allow us to attribute the poor spectra in the rectangular-shaped and hexagonal-shaped ring structures to over-coupling and those in the circular-shaped ring resonator to under-coupling between the ring and the bottom waveguide.

According to Fig. 11, the modified racetrack-shaped ring, with the straight-waveguide length of $L = 100$ nm and other parameters unchanged, is simulated and the results are shown in Fig. 12. One can see that the transmittance spectra in Fig. 12(a) now have all the resonant dips reaching nearly 0% transmittance, compared to Fig. 10(a). Notice that the resonant dips in Fig. 12(a) are shifted a little to left, compared with those in Fig. 10(a), because the ring circumference is now larger than the original circular one by 200 nm. The Q-factors for the four dips in Fig. 12(a) are 234, 170, 95, and 60, respectively, and

TABLE II
COMPARISON OF STRUCTURAL PARAMETERS (IN NANOMETERS) AND TRANSMITTANCES AT RESONANT DIPS AMONG FOUR PLASMONIC RINGS

Ring shape	Guide width	Gap	Ring size	Transmittances at resonant dips
Square	50	20	L=725	0.003/0.008/0.49/0.15/0.32/0.27/0.03
Hexagonal	100	20	R=450	0.07/0.17/0.19/0.07/0.03/0.06
Circular	100	20	R=500	0.15/0.09/0.1/0.03
Racetrack	100	20	R=500	0.001/0.003/0.002/0.0001

the FSRs are 177.5, 116.6, and 81.9 nm. Since we have optimized the spectrum, we can now show the possible influence if the second (upper) waveguide as in dielectric ring is added to the plasmonic racetrack-shaped ring resonator. Fig. 12(b) shows the spectra for one- and two-waveguide structures. Apparently, the two-waveguide structure possesses a similar spectrum to that of the one-waveguide structure, but the extinction ratio is much poorer. This can be understood by the fact that waves will propagate to the "Drop port" due to the existence of the second waveguide so that fewer waves are reserved inside the ring and will then cause insufficient interference at the "Throughput port." This gives the reason why the notch-type structure is used for the plasmonic ring resonator.

The field distributions for both ON-resonance and OFF-resonance at the resonant frequencies 326.73 and 272.53 THz are shown in Fig. 12(c) and (d), respectively. Besides the much better characteristics in transmittance spectra of Fig. 12(a), we can see from Fig. 12(c) that the field strength in the bottom waveguide at ON-resonance is closer to that in Fig. 12(d) at OFF-resonance, indicating that there are just few waves being coupled to backward propagation.

Table II summarizes structural parameters, including waveguide width, gap, and ring dimension, and the PSTD calculated transmittances at resonant dips of the four plasmonic ring resonators discussed previously for comparison. Except the geometry of square ring is as defined in [16], differences between different ring structures are in fact small, but apparently the racetrack-shaped ring provides nearly zero transmittance at four resonant dips, which is better than the other three rings.

We have mentioned earlier that the transmittance spectra for all plasmonic ring resonators shown above are depicted with both Drude and Drude–Lorentz models. In all relevant plots, the two curves are almost overlapped in the lower frequency region, but the Drude–Lorentz curve appears to have lower transmittance in the higher frequency region with the resonant dips shifted slightly to the left. This can be understood from our curve-fitting of the dispersive characteristics for silver in Fig. 1: for the curves of the real part of the relative permittivity, the two models fit differently in the higher frequency part, resulting in different propagation constants, or waveguide wavelengths, and thus shifted resonant dips; on the other hand, larger imaginary part of the relative permittivity in the Drude–Lorentz model leads to higher attenuations or propagation losses.

VI. CONCLUSION

We have discussed in this paper several dielectric and plasmonic waveguide-coupled ring resonators, based on numerical simulations of their optical behaviors using the multidomain Legendre PSTD method with curvilinear- quadrilateral subdomain partitioning. Basically, dielectric microrings provide better optical responses, including lower losses, larger extinction ratios, higher finesse, etc, but they are of relatively large footprint with the ring radius on the order of several or tens of micrometers in order to avoid bending losses. In such dielectric-ring structures including the single-ring and double-ring ones, we have presented PSTD simulation results which match very well with the high-accuracy DGTD method [9]. On the contrary, plasmonic-ring resonators can be possibly manufactured on the scale of hundreds of nanometers, which can provide more flexibility and feasibility for designing compact optical circuits and devices. In particular, such plasmonic-ring structures support possible high transmittances of waves passing through sharp bends, making rectangular- and hexagonal-shaped ring structures become functional. In the near-infrared and visible light ranges of the optical spectrum, we show that plasmonic-ring resonators can perform better in transmittance behaviors by further smoothing the bending structures, such as to become circular geometry, to avoid the coupling waves to propagate backward. Furthermore, adding two optimized short sections of straight waveguide to form the racetrack-type ring resonator is demonstrated to offer sufficient coupling length to enhance the extinction ratios and avoid possible over- and under-coupling problems.

The following remarks concern the more practical 3-D device structures. In this paper, 2-D structures were considered to demonstrate the applications of the Legendre PSTD method, in particular, several MDM plasmonic-ring resonators were investigated and compared. The method has already been developed in its 3-D form [7] and its applications to 3-D device structures should be straightforward. Nevertheless, modeling and simulation of 3-D photonic structures have been known to be expensive tasks, at least as far as the large number of unknowns in the problem is concerned. In plasmonic problems, due to the possible strong field localization near the metal–dielectric interfaces, numerical mesh grids have to be finely designed near these interfaces to reveal such field feature, and in 3-D structures, such modeling can be more challenging. In recent development of plasmonic nanocircuits, the 3-D slot waveguide has been a well-adopted structure [23]. It can be considered as a 3-D extension of the MDM waveguide with the metals appearing to be a metallic thin layer on top of a dielectric substrate and an air or dielectric slot made in the metallic layer. Using the PSTD method to obtain high-accuracy simulations of related slot-waveguide-based resonators is under our investigation.

ACKNOWLEDGMENT

The authors would like to thank the National Center for High-Performance Computing in Hsinchu, Taiwan, and the Academia Sinica Computing Center in Taipei, Taiwan, for providing useful computing resources.

REFERENCES

[1] A. Taflove and S. C. Hagness, *Computational Electrodynamics: The Finite-Difference Time-Domain Method*, 3rd ed. Norwood, MA: Artech House, 2005.
[2] D. G. Rabus, *Integrated Ring Resonators: The Compendium*. Berlin, Germany: Springer-Verlag, 2007.
[3] K. Chang and L. H. Hsieh, *Microwave Ring Circuits and Related Structures*, 2nd ed. Hoboken, NJ: Wiley, 2004.

[4] S. Dey and R. Mittra, "A locally conformal fnite-difference time-domain algorithm for modeling three-dimensional perfectly conducting objects," *IEEE Microw. Guided Wave Lett.*, vol. 7, no. 9, pp. 273–275, Sep. 1997.
[5] Y. Liu, C. D. Sarris, and G. V. Eleftheriades, "Triangular-mesh-based FDTD analysis of two-dimensional plasmonic structures supporting backward waves at optical frequencies," *J. Lightw. Technol.*, vol. 25, no. 3, pp. 938–945, Mar. 2007.
[6] Y. Zhao and Y. Hao, "Finite-difference time-domain study of guided modes in nano-plasmonic waveguides," *IEEE Trans. Antennas Propag.*, vol. 55, no. 11, pp. 3070–3077, Nov. 2007.
[7] C. H. Teng, B. Y. Lin, H. C. Chang, H. C. Hsu, C. N. Lin, and K. A. Feng, "A Legendre pseudospectral penalty scheme for solving time-domain Maxwell's equations," *J. Sci. Comput.*, vol. 36, pp. 351–390, 2008.
[8] W. J. Gordon and C. A. Hall, "Transfinite element methods: Blending-function interpolation over arbitrary curved element domains," *Numer. Math.*, vol. 21, pp. 109–129, 1973.
[9] X. Ji, T. Lu, W. Cai, and P. Zhang, "Discontinuous Galerkin time domain (DGTD) methods for the study of 2-D waveguide-coupled microring resonators," *J. Lightw. Technol.*, vol. 23, no. 11, pp. 3864–3874, Nov. 2005.
[10] S. C. Hagness, D. Rafizadeh, S. T. Ho, and A. Taflove, "FDTD microcavity simulations: Design and experimental realization of waveguide-coupled single-mode ring and whispering-gallery-mode disk resonators," *J. Lightw. Technol.*, vol. 15, no. 11, pp. 2154–2164, Nov. 1997.
[11] A. Belarouci, K. B. Hill, Y. Liu, Y. Xiong, T. Chang, and A. E. Craig, "Design and modeling of waveguide-coupled microring resonator," *J. Lumin.*, vol. 94–95, pp. 35–38, 2001.
[12] B. E. Little, S. T. Chu, H. A. Haus, J. Foresi, and J.-P. Laine, "Microring resonator channel dropping filters," *J. Lightw. Technol.*, vol. 15, no. 6, pp. 998–1005, Jun. 1997.
[13] S. I. Bozhevolnyi, V. S. Volkov, E. Devaux, J. Y. Laluet, and T. W. Ebbesen, "Channel plasmon subwavelength waveguide components including interferometers and ring resonators," *Nature*, vol. 440, no. 23, pp. 508–511, Mar. 2006.
[14] S. Xiao, L. Liu, and M. Qiu, "Resonator channel drop filters in a plasmon-polaritons metal," *Opt. Exp.*, vol. 14, pp. 2932–2937, Jan. 2006.
[15] N. Talebi, A. Mahjoubfar, and M. Shahabadi, "Plasmonic ring resonator," *J. Opt. Soc. Amer. B*, vol. 25, no. 12, pp. 2116–2122, Dec. 2008.
[16] A. Hosseini and Y. Massoud, "Nanoscale surface plasmon based resonator using rectangular geometry," *Appl. Phys. Lett.*, vol. 90, pp. 181102-1–181102-3, Apr. 2007.
[17] Z. H. Han, E. Y. Pun, and S. He, "Plasmonic waveguide resonators based on hexagonal structures," presented at the presented at the Integr. Photon. Nanophoton. Res. Appl., OSA Tech. Digest (CD), Honolulu, HI, 2009, Paper IWC8.
[18] S. A. Maier, *Plasmonics: Fundamentals and Applications*. Berlin, Germany: Springer-Verlag, 2007.
[19] G. Veronis and S. Fan, "Bends and splitters in metal-dielectric-metal subwavelength plasmonic waveguides," *Appl. Phys. Lett.*, vol. 87, pp. 131102-1–131102-3, Sep. 2005.
[20] A. Vial, A. S. Grimault, D. Macias, D. Barchiesi, and M. L. D. L. Chapelle, "Improved analytical fit of gold dispersion: Application to the modeling of extinction spectra with a finite-difference time-domain method," *Phys. Rev. B*, vol. 71, pp. 085416-1–085416-7, Feb. 2005.
[21] P. B. Johnson and R. W. Christy, "Optical constants of the noble metals," *Phys. Rev. B*, vol. 6, pp. 4370–4379, Dec. 1972.
[22] M. H. Carpenter and C. A. Kennedy, Fourth order 2N-storage Runge–Kutta scheme NASA, Hampton, VA, NASA-TM-109112, 1994.
[23] W. Cai, W. Shin, S. Fan, and M. L. Brongersma, "Elements for plasmonic nanocircuits with three-dimensional slot waveguides," *Adv. Mater.*, vol. 22, pp. 5120–5124, 2010.

Shih-Yung Chung received the B.S. degree from the Department of Electrical Engineering, National Cheng Kung University, Tainan, Taiwan, in 2004, and the M.S. degree from the Graduate Institute of Electronics Engineering, National Taiwan University, Taipei, Taiwan, in 2006, where he is currently working toward the Ph.D. degree at the Graduate Institute of Electronics Engineering.

His current research interests include the electromagnetic simulations using the pseudospectral time-domain method.

Chih-Yu Wang received the B.S. degree from the Department of Engineering Science, National Cheng Kung University, Tainan, Taiwan, in 2004, and the M.S. degree from the Graduate Institute of Electronics Engineering, National Taiwan University, Taipei, Taiwan, in 2006, where she is currently working toward the Ph.D. degree at the Graduate Institute of Electronics Engineering.

Her current research interests include the pseudospectral electromagnetics modeling in frequency domain.

Chun-Hao Teng was born in Tainan, Taiwan, on February 14, 1970. He received the diploma in mechanical engineering from the National Taipei Institute of Technology, Taipei, Taiwan, in 1990, and the M.S. degree in mechanical engineering from Clarkson University, Potsdam, NY, in 1996, and the M.S. and Ph.D. degrees in applied mathematics from Brown University, Providence, RI, in 2001.

From 2003 to 2009, he was an Assistant Professor in the Department of Mathematics, National Cheng Kung University, Tainan, Taiwan. He is currently an Assistant Research Fellow at the Center of Mathematical Modeling and Scientific Computing, National Chiao Tung University, Hsinchu, Taiwan. His research interests include the developments and applications of high-order numerical methods for partial differential equations.

Chung-Ping Chen (M'96) received the B.S. degree in computer science and information engineering from National Chiao-Tung University, Hsinchu, Taiwan, in 1990, and the M.S. and Ph.D. degrees in computer science from the University of Texas, Austin, in 1996 and 1998, respectively.

From 1996 to 1999, he was with Strategic Computer-Aided Design (CAD) Labs, Intel Corporation, Hillsboro, OR, as a Senior CAD Engineer. Since 1999, he has been an Assistant Professor with the Department of Electrical and Computer Engineering, University of Wisconsin, Madison. Since 2003, he has also been an Associate Professor with the Electrical Engineering Department, National Taiwan University, Taipei, Taiwan, where he is also a Professor with the Graduate Institute of Electronics Engineering, Biomedical Electronics and Bioinformatics and Electrical Engineering Departments. His research interests include the areas of electronic design automation and BIO topics, including CAD and microprocessor circuit design with an emphasis on interconnect and circuit optimization, circuit simulation, statistical design, and signal/power/thermal integrity analysis and optimization.

Dr. Chen received the D2000 Award from Intel Corporation and the National Sciences Foundation Faculty Early Career Development awards (CAREER) from 1999 to 2001, respectively. He also received the 2002 Special Interest Group on Design Automation/ACM Outstanding Young Faculty Award and the 2002 IBM Peter Schneider Faculty Development Award. He served the program committee and is an organizer of the Design Automation Conference, the International Conference on Computer-Aided Design, Design, Automation, and the Test in Europe Conference, the International Symposium on Physical Design, the Asia and South Pacific Design Automation Conference, the International Symposium on Quality Electronic Design, Synthesis and System Integration of Mixed Information, the VLSI/CAD Symposium, and the International Technology Roadmap for Semiconductors Conference.

Hung-Chun Chang (S'78–M'83–SM'00) was born in Taipei, Taiwan, on February 8, 1954. He received the B.S. degree from National Taiwan University, Taipei, in 1976, and the M.S. and Ph.D. degrees from Stanford University, Stanford, CA, in 1980 and 1983, respectively, all in electrical engineering.

From 1978 to 1984, he was with the Space, Telecommunications, and Radioscience Laboratory of Stanford University. In August 1984, he joined the Faculty of the Electrical Engineering Department of National Taiwan University, where he is currently a Distinguished Professor. He was the NTU Himax Chair Professor during 2011. He served as Vice-chairman of the Department of Electrical Engineering from 1989 to 1991, and Chairman of the newly established Graduate Institute of Electro-Optical Engineering at the same University from 1992 to 1998. His current research interests include the electromagnetic theory, design, and application of photonic structures and devices for fiber optics, integrated optics, optoelectronics, nanophotonics, and plasmonics.

Dr. Chang served as the Institute of Electronics, Information and Communication Engineers (Japan) Overseas Area Representative in Taipei from 2002 to 2007. He is a Fellow of the Optical Society of America and the Electromagnetics Academy.